Annales Geophysicae

Excitation of the ionospheric resonance cavity by neutral winds at middle latitudes

V. V. Surkov[1]**, O. A. Pokhotelov**[2]**, M. Parrot**[3]**, E. N. Fedorov**[2]**, and M. Hayakawa**[4]

[1]Moscow State Engineering Physics Institute, 115409, Moscow, 31 Kashirskaya road, Russia
[2]Institute of Physics of the Earth, 123995 Moscow, 10 Bolshaya Gruzinskaya str., Russia
[3]Laboratoire de Physique et Chimie de l'Environnement, Centre National de la Recherche Scientifique, Orléans, France
[4]The University of Electro-Communications, Chofu, Tokyo, Japan

Abstract. A new mechanism for the ionospheric Alfvén resonator (IAR) excitation at middle latitudes is considered. It is shown that the ionosphere wind system in this region is capable of sustaining the generation of geomagnetic perturbations that can be detected by ground magnetometers. The general IAR dispersion relation describing the linear coupling of the shear Alfvén and fast magnetosonic/compressional modes is obtained. The dependence of the IAR eigenfrequencies and damping rates on the perpendicular wave number and on the ground conductivity during the day- and nighttime conditions is analyzed both analytically and numerically. In order to demonstrate the IAR excitation by neutral winds the power spectra of the geomagnetic perturbation on the ground surface are calculated. Furthermore, it is found that Kolmogorov spectra of the ionospheric turbulent neutral winds and the IAR eigenfrequencies lie in the same frequency range that make it possible to enhance the IAR excitation. The relevance of the developed theoretical model to the ground-based observations is stressed.

Key words. Ionosphere (Ionosphere-atmosphere interactions; mid-latitude ionosphere; plasma waves and instabilities)

1 Introduction

The low-frequency electromagnetic (EM) perturbations in the frequency range of $10^{-3}-10$ Hz are of special interest in geophysical studies (e.g. Kangas et al., 1998). Nearly all magnetospheric and ionospheric resonances fall in this class. Among them are the MHD resonances of the magnetosphere as a whole, the field-line resonances and Shumann resonances of the Earth-ionosphere cavity ($f \sim 8$ Hz). This frequency range is associated with the operation of the so-called Alfvén masers generating the ion-cyclotron waves in the Earth's magnetosphere (Andronov and Trakhtengertz,

1964; Bespalov and Trakhtengertz, 1986) which define the characteristic lifetime of the trapped radiation (Kennel and Petschek, 1966).

A special credit has been paid in the past to the study of the ionospheric Alfvén resonator (IAR) that arises due to a strong increase in the Alfvén wave refractive index in the ionosphere (Polyakov, 1976; Polyakov and Rapoport, 1981). The resonator lower boundary coincides with the E-layer where nearly all plasma parameters undergo a strong jump. The upper boundary is located at a few thousands of kilometers from the Earth's surface due to the reflection of the IAR eigenmodes caused by a nearly exponential decrease in plasma density above the maximum of the F-layer. The latter results in the violation of the WKB approximation and partial wave reflections that form a resonance cavity in the topside ionosphere. The same cavity serves as the waveguide for the fast/compressional mode.

The existence of the IAR was well documented by ground-based observations both in middle (Polyakov and Rapoport, 1981; Belyaev et al., 1987, 1990; Hickey et al., 1996; Bösinger et al., 2002) and in high latitudes (Belyaev et al., 1999; Demekhov et al., 2000). The resonator was also identified in the Freja and FAST data (e.g. Grzesiak, 2000; Chaston et al., 1999, 2002, 2003). The basic mechanism of the IAR excitation at high latitudes usually refers to the development of the fast feedback instability induced by the large-scale ionospheric shear flows (Lysak, 1991; Trakhtengertz and Feldstein, 1991; Pokhotelov et al., 2000, 2001). The energetics of this instability was reviewed by Lysak and Song (2002). The nonlinear theory of the IAR was recently developed by Pokhotelov et al. (2003, 2004) and Onishchenko et al. (2004).

It should be noted that the feedback instability can serve as the basic mechanism of the IAR excitation at high latitudes where the convection electric fields can reach quite strong values. On the contrary, at middle latitudes other sources of the free energy can come into play. For example, generation of the IAR can be associated with the thunderstorm activity (e.g. Polyakov and Rapoport, 1981; Belyaev et al.,

---

Correspondence to: M. Parrot
(mparrot@cnrs-orleans.fr)
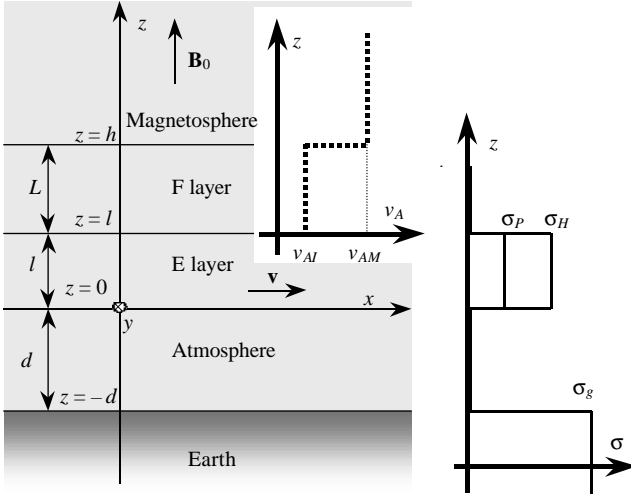
Fig. 1. A schematic drawing of a stratified medium model. The plots of the Alfvén velocity and the ionosphere/ground conductivities are shown in the right panel.

1987, 1990). In some cases the IAR manifests itself as the anomalous ULF transients and can be observed in the upper ionosphere on board the low-orbiting satellites above strong atmospheric weather systems (Fraser-Smith, 1993). In due time Sukhorukov and Stubbe (1997) considered the nonlinear conversion of the lightning discharges' energy into the IAR eigenmodes.

We note that at middle latitudes there is a natural source of free energy stored in the ionospheric neutral wind motions which can excite the IAR similar to the operation of a police whistle. The consideration of this new mechanism is the subject of the present study.

The paper is organized in the following fashion: Our model and the basic equations describing the IAR in the presence of the neutral winds are presented in Sect. 2. The boundary conditions for the IAR are formulated in Sect. 3. In Sect. 4 the dispersion relation for two coupled modes is examined, and the IAR eigenfrequencies are found. Section 5 is devoted to the study of excitation of the resonance cavity by the high-altitude neutral winds. We complete the paper with our discussion and conclusions in Sect. 6. The Appendices A–C contain the details of our analytical calculations.

2 The model and basic equations

It is common knowledge that the ionospheric resonance cavity is localized at altitudes below $1-2\,R_E$. At such small altitudes the magnetic field line curvature is of little importance and thus neglected. On the contrary, the plasma number density, the collision frequencies, the plasma conductivity and other parameters exhibit strong variations inside the IAR. A schematic drawing of our model is shown in Fig. 1. The gyrotropic E-layer of the ionosphere is bounded by $z=0$

and $z=l$. Due to the high mobility of the electrons along the magnetic field lines the parallel conductivity is high and thus $\sigma_\parallel \to \infty$. The latter condition shortcuts the wave parallel electric field, i.e. $E_z=0$ at least when the waves' length is larger than the inertial electron skin depth. Furthermore, the plasma is assumed to be uniform within each layer in the direction perpendicular to the external magnetic field. For the sake of simplicity we adopt the model of the vertical external magnetic field in order to avoid the complexities connected with magnetic field inclination.

We start from Ohm's law for the conductive ionospheric E-layer given by (e.g. Kelley, 1989)

$$\mathbf{j}_\perp = \sigma_P \mathbf{E}'_\perp + \sigma_H \widehat{\mathbf{z}} \times \mathbf{E}'_\perp, \tag{1}$$

where σ_H and σ_P are the Hall and Pedersen conductivities, $\mathbf{E}' = \mathbf{E} + \mathbf{v} \times \mathbf{B}$, $\mathbf{E}$ is the wave electric field, $\mathbf{B}$ is the external magnetic field which is directed along the z-axis, $\mathbf{v}$ is the neutral wind velocity, $\widehat{\mathbf{z}} = \mathbf{B}/B$ and the subscript $\perp$ denotes the component perpendicular to $\mathbf{B}$. For clarity we consider that the stationary convective electric field is absent, and the EM perturbations are solely due to the neutral wind. Within the altitudes of the E-layer the ratio of plasma to neutral number densities is $\sim 10^{-7}-10^{-9}$ for the day- and nighttime conditions, respectively. Based on this value one can find that the influence of the motions of the electrons and ions on the wind motion is negligible. Therefore, we can consider the neutral wind velocity $\mathbf{v}$ in the E-layer as a given function, that can serve as a source for the EM perturbations.

The dynamics of the plasma number density variations δn in the ionospheric E-layer governs by

$$\partial_t \left(\frac{\delta n}{n} - \frac{\delta B_\parallel}{B} \right) = \frac{j_\parallel}{enl} + \nu \frac{\delta n}{n}, \tag{2}$$

where, contrary to the high altitudes, the effects due to the energetic electron precipitations are neglected. Furthermore, $\partial_t \equiv \partial/\partial t$, $n \approx 10^{11}\,\mathrm{m}^{-3}$ is the ambient plasma number density, e is the magnitude of the electron charge, $\delta B_\parallel$ is the compressional variation of the magnetic field, $l \approx 30 - -40\,\mathrm{km}$ is the reduced scale of the E-layer, $j_\parallel$ is the field-aligned electric current and $\nu \approx 6 \times 10^{-3}\,\mathrm{s}^{-1}$ is the recombination rate.

With the help of Ampère's law and the condition $\Delta \cdot \delta \mathbf{B}$ one can verify that the field-aligned current scales as $j_\parallel \propto \mu_0^{-1} (\delta B_\parallel / l)$. For the wave frequencies of the order of 1 Hz the terms on the right-hand side of Eq. (2) are of two orders smaller than those on the left and thus the variation of the plasma density scales as $\delta n/n \propto \delta B_\parallel/B$. Using this relation and the explicit expression for the perpendicular electric current Eq. (1) one can estimate the relative importance of the plasma density variations in the Ampère's law which is controlled by the following dimensionless parameter

$$\epsilon = \frac{\sigma_P |\mathbf{E}_\perp|}{\delta \sigma_P v_0 B} \approx \frac{n}{\delta n} \frac{|\mathbf{E}_\perp|}{B v_0} \approx \frac{v_{AI}}{v_0} \frac{1}{kl}, \tag{3}$$

where $v_0 \approx 100\,\mathrm{m/s}$ is the typical wind velocity, $\delta \sigma_P$ is variation of the ionospheric conductivity, $v_{AI} \approx 500\,\mathrm{km/s}$ is the

Alfvén velocity in the E-layer and k is the perpendicular wave number. When $kl \gtrsim 1$ the magnetic perturbations are completely "screened" by the ionosphere and are not seen on the ground. Since in what follows we will be interested solely in ground measurements, we restrict our consideration to the case $kl \lesssim 1$. In this particular case $\epsilon \gg 1$, and the variations of the ionospheric plasma density that enter the Ampère's law can be neglected. They simply follow the compressional variations of the magnetic field, i.e. $\delta n/n \approx \delta B_{\parallel}/B$. Thus, in our approximation in the wave equations that will be derived below, the Hall and Pedersen conductivities can be treated as constant quantities. The opposite case $kl \gtrsim 1$ has been recently analyzed numerically by Streltsov and Mishin (2003), in connection with interpretation of EM wave structures observed by the Defence Meteorological Satellite Programme (DMSP) during a magnetic storm within subauroral polarization streams (Mishin et al., 2003).

To describe the EM perturbations we make use of the standard two-potential (Φ, Ψ) representation, that is,

$$\mathbf{E}_{\perp} = -i\omega \left(\frac{\mathbf{k}\Phi}{\omega} - i\mathbf{k} \times \hat{\mathbf{z}}\Psi \right),$$ (4)

$$\delta\mathbf{B} = \partial_z \left(\frac{\mathbf{k} \times \hat{\mathbf{z}}}{\omega} \Phi + i\mathbf{k}\Psi \right) + k^2 \Psi \hat{\mathbf{z}}.$$ (5)

All perturbed quantities are considered to vary as $\exp(-i\omega t + i\mathbf{k} \cdot \mathbf{r})$, where ω and $\mathbf{k}$ are the wave frequency and the perpendicular wave vector, $\delta\mathbf{B}$ is the perturbation of the magnetic field and $\partial_z \equiv \partial/\partial z$.

Since in our model $E_z = 0$, the z-component of the vector potential is connected through the z-derivative of Φ by the relation $A = -i\omega^{-1}\partial_z\Phi$ and thus eliminated from Eq. (5).

Using Eqs. (1)–(5), from Ampère's law we obtain a system of two differential equations for Φ and Ψ that describes the coupling of the ionospheric MHD modes with neutral wind motions

$$\partial_z^2\Phi + i\mu_0\omega\sigma_P\Phi + \mu_0\omega^2\sigma_H\Psi$$
$$= \frac{B\mu_0\omega}{k^2} \left[\sigma_P(\mathbf{k} \times \mathbf{v})_z + \sigma_H(\mathbf{k} \cdot \mathbf{v}) \right],$$ (6)

$$\partial_z^2\Psi - \left(k^2 - i\mu_0\omega\sigma_P \right)\Psi + \mu_0\sigma_H\Phi =$$
$$-\frac{iB\mu_0}{k^2} \left[\sigma_H(\mathbf{k} \times \mathbf{v})_z - \sigma_P(\mathbf{k} \cdot \mathbf{v}) \right].$$ (7)

In our model the region $z > l$ above the E-layer is supposed to be the area consisting solely of cold collisionless plasma. The plasma dielectric tensor in this region is assumed to be diagonal with the components $\varepsilon_{\parallel}$ and $\varepsilon_{\perp}$. The Alfvén velocity can be expressed through $\varepsilon_{\perp}$, i.e. $v_A = c\varepsilon_{\perp}^{-\frac{1}{2}}$, where c is the speed of light. In the ionospheric resonance cavity the Alfvén velocity increases with the altitude z due to a strong decrease in the ionosphere plasma density. Such a dependence can be approximated by a simple analytical exospheric profile (e.g. Greifinger and Greifinger, 1968), that is,

$$v_A^2 = v_{A0}^2 \left\{ \varepsilon^2 + \exp\left[-2\left(z - l \right)/L \right] \right\}^{-1}, \qquad z \geq l,$$ (8)

where $v_{A0} \approx 500$ km/s is the Alfvén velocity at the bottom of the resonance cavity, $\varepsilon \approx 0.01$ is a small, dimensionless parameter and $L \approx 10^3$ km is the typical vertical scale of the resonator.

The velocity profile Eq. (8) is quite close to the model is ionospheric numerical profiles and can be considered as representative. The use of such an analytical approximation makes it possible to express the IAR eigenfunctions in terms of Bessel functions and to obtain simple analytical expressions for the eigenfrequencies and the IAR damping/growth rates.

In order to make our consideration as transparent as possible, we choose a simplified approximation (e.g. Pokhotelov et al., 2001). which describes the Alfvén velocity in terms of a piece-wise function, so that $v_A = v_{AI}$ within the F-layer of the ionosphere ($l < z < h = l + L$) and $v_A = v_{AM}$ in the magnetosphere ($z > h$), where v_{AI} and v_{AM} ($v_{AM} \gg v_{AI}$) are constant quantities (see Fig. 1), i.e. $v_{AI} \approx v_{A0}$ and $v_{AM} \approx v_{A0}\varepsilon^{-1}$.

For the altitudes $z > l$ the conductivity tensor entering Ampère's law should be replaced by the tensor of dielectric permittivity. Combining Ampere's law and Eqs. (4)–(5) we arrive at the wave equations for the shear Alfvén and fast modes in the region $z > l$

$$\partial_z^2\Phi + \frac{\omega^2}{v_A^2}\Phi = 0,$$ (9)

$$\partial_z^2\Psi - \lambda^2\Psi = 0, \qquad \lambda = \left(k^2 - \omega^2/v_A^2 \right)^{\frac{1}{2}}.$$ (10)

Here $v_A = v_{AI}$ when $l < z < h$ and $v_A = v_{AM}$ when $z > h$. The solutions of these equations have to be continuous at $z = h$. When $z > h$ the solution of Eq. (9) in the form of an outgoing Alfvén wave should be retained. Moreover, Ψ has to be limited at infinity ($z \to \infty$). The solution of Eqs. (9) and (10) that satisfy such boundary conditions are given in Appendix A. The boundary condition at the lower end, $z = l$, of the IAR is considered in the next section.

The neutral atmosphere ($-d < z < 0$) is considered as a vacuum region, and the solid Earth ($z < -d$) as a uniform conductor with a constant conductivity σ_g. Since the resistance between the ionosphere and the ground is much greater than that of the ionosphere, one can neglect the field-aligned current flowing from the ionosphere to the atmosphere, and at $z = 0$ (the boundary between the ionosphere and atmosphere) we set $j_z(0) = 0$, which, according to Eq. (5), assumes that $\partial_z\Phi = 0$. Thus, Φ is a constant quantity in the atmospheric layer which, for simplicity, we set to zero, and Ψ satisfies the Laplace equation, that is,
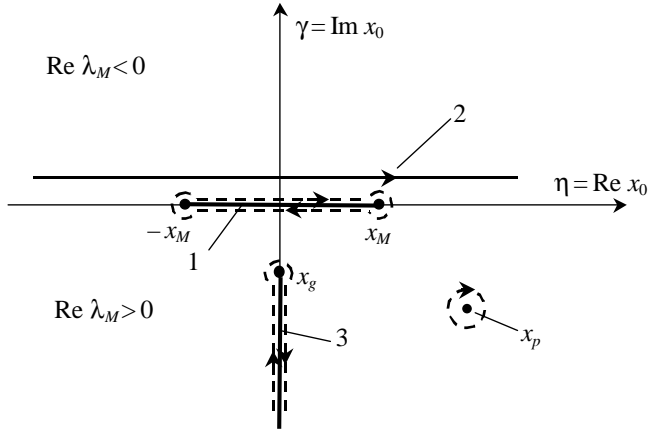
$$\partial_z^2\Psi - k^2\Psi = 0, \qquad -d < z < 0.$$ (11)

Similarly for the solid Earth ($z < -d$) we have

$$\partial_z^2\Psi - æ^2\Psi = 0,$$ (12)

where $æ^2 = k^2 - i\mu_0\omega\sigma_g$.

The above obtained equations should be supplemented by relevant boundary conditions that follow from Ampère's law

Fig. 2. A sketch of a complex x_0 plane. 1 – a cut in the complex plane that connects the bifurcation points of λ_M. 2 – an integration path for the inverse Fourier transform. 3 – a cut for æ. One of the poles of the integrand is shown with x_p.

and require that the scalar potentials, Φ and Ψ, and their first derivatives, $\partial_z \Phi$ and $\partial_z \Psi$, be continuous at all boundaries, that is, at $z=-d$, $z=0$, $z=l$ and $z=h$. In greater detail they are examined in Appendices A and B.

3   Magnetic field perturbation on the Earth's surface

Since below the conductive slab Φ vanishes the perturbation of the magnetic and electric fields on the ground can be expressed solely through Ψ at $z=-d$, that is, $\delta\mathbf{B}=i\mathbf{k}\partial_z\Psi+k^2\Psi\hat{\mathbf{z}}$ and $\mathbf{E}_\perp=\omega\Psi\hat{\mathbf{z}}\times\mathbf{k}$. Furthermore, according to Eq. (12) on the ground $\partial_z\Psi(-d)=æ\Psi(-d)$. Hence the magnetic and electric fields on the solid Earth are

$$\delta\mathbf{B} = \left(i\mathbf{k}æ + k^2\hat{\mathbf{z}}\right)\Psi(-d), \qquad \mathbf{E}_\perp = \omega\hat{\mathbf{z}}\times\mathbf{k}\Psi(-d)\,. \,(13)$$

Substitution of the explicit expression for $\Psi(-d)$ into Eq. (13) gives

$$\delta\mathbf{B}/B = \frac{Q\left(\hat{\mathbf{z}} + i\mathbf{k}æ/k^2\right)}{\beta_3\left[(is + x_0\alpha_P)(\beta_1 + \alpha_P) + x_0\alpha_H^2\right]}\,. \qquad (14)$$

Here we made use of the following abbreviations

$$Q=Lv_{AI}^{-1}\left[(\mathbf{k}\cdot\mathbf{v})\left(\alpha_H^2 + \alpha_P^2 + \beta_1\alpha_P\right) - (\mathbf{k}\times\mathbf{v})_z\beta_1\alpha_P\right] \quad (15)$$

$$s = (kL)\frac{æ + k\tanh(kd)}{k + æ\tanh(kd)} - \lambda_I\beta_2, \qquad (16)$$

$$\beta_1 = \frac{1 + \varepsilon - (1 - \varepsilon)\exp(2ix_0)}{1 + \varepsilon + (1 - \varepsilon)\exp(2ix_0)}, \qquad (17)$$

$$\beta_2 = \frac{\lambda_I + \lambda_M - (\lambda_I - \lambda_M)\exp(2\lambda_I)}{\lambda_I + \lambda_M + (\lambda_I - \lambda_M)\exp(2\lambda_I)}, \qquad (18)$$

$$\beta_3 = \cosh(kd) + \frac{æ}{k}\sinh(kd)\,, \qquad (19)$$

where $x_0=\omega L/v_{AI}$ is the dimensionless IAR frequency, $\alpha_P=\Sigma_P/\Sigma_w$ and $\alpha_H=\Sigma_H/\Sigma_w$ stand for the dimensionless height-integrated Pedersen and Hall conductivities, respectively, $\Sigma_w=1/\mu_0 v_{AI}$ is the Alfvén parallel conductance, $\varepsilon=v_{AI}/v_{AM}$, $\lambda_I=(k^2L^2-x_0^2)^{1/2}$ and $\lambda_M=(k^2L^2-x_0^2\varepsilon^2)^{1/2}$.

4   The general IAR dispersion relation

The IAR eigenfrequencies are defined by the zeros of the denominator in Eq. (14)

$$(is + x_0\alpha_P)(\beta_1 + \alpha_P) + x_0\alpha_H^2 = 0\,. \qquad (20)$$

To analyze this dispersion relation it is necessary to specify the signs of λ_M, λ_I and æ. The function λ_M in Eq. (18) has two bifurcation points $x_0=\pm x_M$, where $x_M=kL/\varepsilon$. To specify the sign of this function we make a cut in the complex plane x_0 shown in Fig. 2 with line 1. As k is purely real, the imaginary part of λ_M equals zero along the cut that connects two bifurcation points, as well as on the vertical line where $\text{Re}\,x_0=0$. In order to satisfy the so-called radiation condition at infinity we choose the physical sheet of Riemann's surface. In this case $\text{Im}\,\lambda_M>0$ on the right semi-space and $\text{Im}\,\lambda_M<0$ on the left one. The real part of λ_M is positive on the lower semi-space (what does hemiplande mean?) and it has the opposite sign in the upper space. The integration path for the inverse Fourier transform is shown in Fig. 2 with line 2.

The function s on the left-hand side of Eq. (20) is an even function of λ_I. Thus, the bifurcations of the function λ_I can be left out. The function æ has the only bifurcation point $x_0=x_g$, where $x_g=-ik^2L\Sigma_w/\sigma_g$. The cuts in the complex plane x_0 are chosen to coincide with the lines on which $\text{Re}\,æ=0$ (Fig. 2, line 3). In addition, we require that the condition $\text{Re}\,æ\geq0$ holds everywhere.

In what follows, we will show that the roots of Eq. (20) lie in the lower part of the complex plane of x_0, where $\text{Re}\,\lambda_M>0$, i.e. they are on the non-physical part of the complex plane. We do not discuss this problem in more detail since it is of importance solely in the region $z>h$, i.e. in the magnetosphere, while our interest refers solely to the magnetic field on the ground.

4.1   Shear Alfvén mode. The zero Hall conductance

We start our analysis with the simplified case of the zero Hall conductance, $\Sigma_H=0$. The general dispersion relation Eq. (20) in this case decouples into two modes. The first one corresponds to the roots of the following equation

$$\beta_1 + \alpha_P = 0. \qquad (21)$$

The eigenmodes of dispersion relation (21) do not depend on k and correspond to the shear Alfvén mode. Indeed, Eq. (21) can be rewritten as

$$\exp(2ix_0) = \left(\frac{1+\varepsilon}{1-\varepsilon}\right)\frac{(1+\alpha_P)}{(1-\alpha_P)}\,, \qquad (22)$$

and thus coincides with Eq. (27) of Pokhotelov et al. (2001). Decomposing the dimensionless frequency in Eq. (22) into

its real and imaginary parts, $x_0 = \eta + i\gamma$, one finds the solution of Eq. (22) in the form

$$\eta = \pi(n-1) + \vartheta_\alpha, \quad \vartheta_\alpha = \frac{1}{2}\arg\frac{(1+\alpha_P)}{(1-\alpha_P)}, \qquad (23)$$

$$\gamma = -\varepsilon - \frac{1}{2}\ln\left|\frac{1+\alpha_P}{1-\alpha_P}\right|, \qquad (24)$$

where n is an integer, $n=1, 2, ...$, $\vartheta_\alpha=0$ when $0\leq\alpha_P<1$ (insulator) and $\vartheta_\alpha=\pi/2$ when $\alpha_P>1$ (conductor).

4.2 Fast mode. The zero Hall conductance

Another family of roots in Eq. (20) corresponds to the fast mode that is described by

$$is + x_0\alpha_P = 0. \qquad (25)$$

Similarly to the previous subsection we rewrite Eq. (25) as

$$\exp(2\lambda_I) = \frac{(\lambda_M + \lambda_I)(\alpha_P + \alpha_g - i\lambda_I/x_0)}{(\lambda_M - \lambda_I)(\alpha_P + \alpha_g + i\lambda_I/x_0)}, \qquad (26)$$

where

$$\alpha_g = \left(\frac{ikL}{x_0}\right)\frac{æ + k\tanh(kd)}{k + æ\tanh(kd)}. \qquad (27)$$

The functions λ_I, λ_M, α_g and therefore the roots of Eq. (26) depend on k, i.e. $x_0=x_0(k)$. The range of very small k or $kL\ll1$, is not of great importance for practical applications. Nevertheless, we notice that the solution of Eq. (26) in this region differs from that (see Eq. (22)) for the shear Alfvén mode even if $k=0$. These solutions coincide only when the ground conductivity is ignored, i.e. $\sigma_g=0$.

Now we examine the opposite case of large k, or more precisely $kL\gg1$. In the first approximation we have $\omega=k/v_{AI}$ or $x_0=kL$ which corresponds to the ordinary dispersion relation for the fast mode in an uniform plasma. It follows from this that in the first approximation $\lambda_I=0$. Notice that formally the value $\lambda_I=0$ satisfies Eq. (26) because in this case both parts of Eq. (26) are equal to unity, but it does not satisfy the original Eq. (25). Thus, in the second approximation, one can find the solution of Eq. (26) in the form

$$x_0 = kL + \delta_1 - i\gamma_1, \qquad (28)$$

where δ_1 and γ_1 are the real parameters to be defined. Moreover, δ_1 and γ_1 are much smaller than kL. These parameters represent small corrections due to the presence of the E-layer with finite thickness and due to the ground conductivity.

Substitution of Eq. (28) into the expression for λ_I, gives

$$\lambda_I \approx [2kL(-\delta_1 + i\gamma_1)]^{1/2}, \quad |\lambda_I| \ll kL. \qquad (29)$$

As it follows from the analysis given below, the real λ_1 and imaginary λ_2 parts of λ_I yield the condition $\lambda_1\ll\lambda_2$. Hence, Eq. (29) reduces to

$$\lambda_I = \lambda_1 + i\lambda_2 = (2kL\delta_1)^{1/2}\left(\frac{\gamma_1}{2\delta_1} + i\right). \qquad (30)$$

Taking into account that the roots of Eq. (26), shown in Fig. 2 by x_p, are in that quarter of a complex plane where the real λ_1 and imaginary λ_2 parts of λ are positive, we find that δ_1 and γ_1 are positive as well.

All other functions in Eqs. (26) and (27) in this approximation should be taken at $x_0=kL$. Hence, $\lambda_M\approx kL$ and

$$æ = æ_0 = \left(k^2 - i\frac{k\sigma_g}{\Sigma_w}\right)^{1/2}.$$

The right-hand side of Eq. (26) can be expressed in terms of a power series in a small parameter λ_I/kL. Thus, Eq. (26) reduces to

$$\exp(2\lambda_I) = 1 + \frac{2\lambda_I}{kL}\left(1 - \frac{i}{\alpha_P + \alpha_0}\right), \qquad (31)$$

where

$$\alpha_0 = i\frac{æ_0 + k\tanh(kd)}{k + æ_0\tanh(kd)}. \qquad (32)$$

The function α_0 can be decomposed into its real and imaginary parts, $\alpha_0=\alpha_1+i\alpha_2$. Equating the moduli and arguments of the functions on both sides of Eq. (31) and then expanding them in a power series of small parameters $\lambda_1/(kL)$ and $\lambda_2/(kL)$, we obtain

$$\lambda_1\left(1 - \frac{a}{kL}\right) = \frac{\lambda_2 b}{kL} \qquad (33)$$

and

$$\lambda_2\left(1 - \frac{a}{kL}\right) = \pi n - \frac{\lambda_1 b}{kL}, \qquad (34)$$

where n is an integer and

$$a = 1 - \frac{\alpha_2}{(\alpha_P + \alpha_1)^2 + \alpha_2^2}, \quad b = \frac{\alpha_P + \alpha_1}{(\alpha_P + \alpha_1)^2 + \alpha_2^2}. \qquad (35)$$

Here the case $n=0$ is excluded since λ_2 is a positive quantity.

The set of Eqs. (33) and (34) defines the functions of sought λ_1 and λ_2. Substituting λ_1 and λ_2 into Eq. (30), one can find δ_1 and γ_1. Finally, with help of Eq. (28), one obtains

$$x_0^n(k) = kL + \frac{\pi^2 n^2}{2kL[1-a/(kL)]^2}\left\{1 - \frac{2bi}{kL[1-a/(kL)]}\right\}, \qquad (36)$$

where a and b are given by Eq. (35). This equation describes the spectrum, $\omega^n(k)=x_0^n(k)v_{AI}/L$, of the damped IAR eigenmodes which corresponds to the fast modes when $kL\gg1$.

4.3 Mode coupling. The role of the ionospheric Hall conductivity

In the above consideration the shear and fast modes remained uncoupled. It is a conventionally idealized model which can be relevant for the nighttime conditions. However, during daytime conditions, the situation may become more complex since the effects due to finite Hall conductivity start to play an important role. This can result in a strong mode coupling. Nevertheless, as before the general dispersion relation
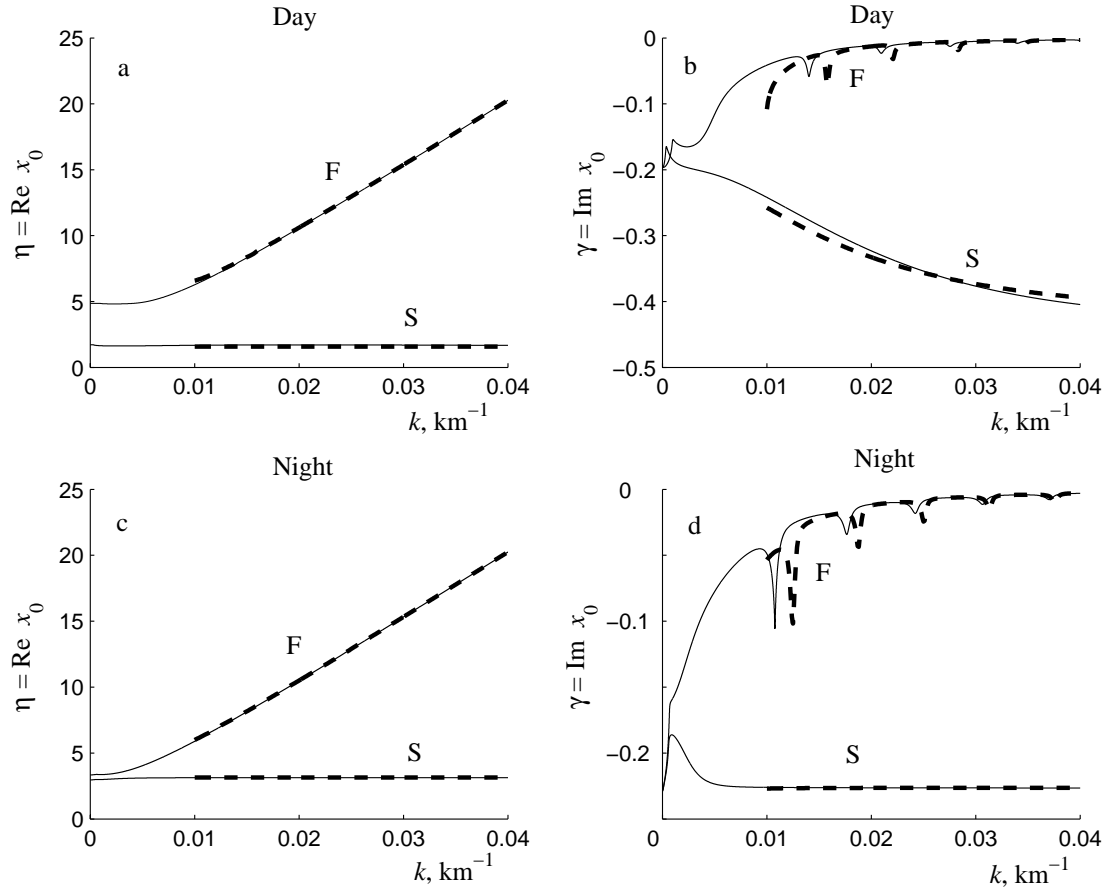
Fig. 3. The plots of the real **(a, c)** and imaginary **(b, d)** parts of the dimensionless frequency x_0 as a function of perpendicular wave number k for the fundamental mode. S and F denote the shear Alfvén and fast modes, respectively. The dashed lines correspond to the approximate analytical formulae.

Eq. (20) consists of two modes. Each mode consists of a discrete set of normal modes. To demonstrate the basic features of the fundamental mode ($n=1$), the numerical analysis of the dispersion relation vs. k Eq. (20) has been carried out. Figures 3a and b show the real and imaginary parts of x_0 as a function of k (in inverse kilometers) for the daytime conditions. A similar plot for the nighttime conditions is depicted in Figs. 3c and d. The numerical values for the various magnetospheric, ionospheric and other parameters are: $v_{AI}=500$ km/s, $v_{AM}=5\times10^3$ km/s, $L=500$ km, $d=100$ km and $\sigma_g=2\times10^{-3}$ S/m. For the daytime ionosphere (Figs. 3a and b) the height-integrated conductivities are $\Sigma_P=5$ Ohm^{-1} and $\Sigma_H=7.5$ Ohm^{-1}, respectively, so that $\alpha_P=3.14$ and $\alpha_H=4.71$. For the nighttime conditions $\Sigma_P=0.2$ Ohm^{-1} and $\Sigma_H=0.3$ Ohm^{-1} (Figs. 3c and d), so that $\alpha_P=0.126$ and $\alpha_H=0.188$.

The real part of x_0 defines the fundamental mode eigenfrequency. The dimensionless eigenfrequency η of the shear Alfvén mode, shown in Figs. 3a and c with solid lines S, practically does not depend on k. At the same time, the fast mode shown in Figs. 3a and c with solid lines F exhibits a linear response to k. Below we will show that this mode tends asymptotically to the dependence $x_0=kL$ or $\omega=kv_{AI}$, which is typical for the fast mode in uniform plasma.

The imaginary part of x_0 or dimensionless attenuation coefficient γ for the fundamental mode is depicted in Figs. 3b and d. One sees that both modes strongly depend on k. Interestingly enough the attenuation of the shear mode (Figs. 3b and d, solid lines S) is much stronger than that for the fast mode (solid lines, F). Certain oscillations, seen in these figures, also distinguish the fast mode from the shear Alfvén mode.

To clarify the mode properties, an explicit solution of the dispersion relation Eq. (20) is required. The necessary approximate dependencies for $x_0(k)$ are given in Appendix C. For the shear Alfvén mode during the daytime we have

$$x_0 = \pi(n-0.5) + i\gamma,\qquad(37)$$

and for the nighttime conditions

$$x_0 = \pi n + i\gamma,\qquad(38)$$

where $n=1, 2, \dots.$

In the first approximation the real part of x_0 thus does not depend on k (Figs. 3a and c, the dashed lines, mode S). This agrees with the numerical calculations of Eq. (20) shown in

Figs. 3a and c with solid line. The imaginary part of x_0, i.e. γ, given by Eq. (C3), can be rewritten as

$$\gamma = -\varepsilon - \frac{1}{4} \ln \left[1 + \frac{4(1 + \mathrm{Re}G)}{|G|^2} \right] . \tag{39}$$

where G

$$G(\eta) = \alpha_P - 1 + \frac{\alpha_H^2}{is(\eta)/\eta + \alpha_P} , \tag{40}$$

and $\eta = \pi(n-1/2)$ or $\eta = \pi n$. For $\alpha_H = 0$ Eq. (39) coincides with Eq. (24). The approximate dependencies Eqs. (39) and (40) (fundamental mode, $n=1$) shown in Figs. 3b and d with the dashed lines (mode S) are close to numerical simulation of Eq. (20).

Now let us consider the fast mode in the limit of large k. The approximate solution is given in Appendix C. The dependence (C13) is obtained in the same manner as it was used in Sect. 4.2. As the parameter $p_1/(kL)$ is neglected, Eq. (C13) reduces to

$$x_0^n = kL + \frac{\pi^2 n^2}{2kL}$$
$$\left\{ 1 - \frac{2[\alpha_P(1+Y) + \alpha_1]i}{kL([\alpha_P(1+Y) + \alpha_1]^2 + [\alpha_2 + Y\tan kL]^2)} \right\} , \tag{41}$$

where α_1 and α_2 stand for the real and imaginary parts of α_0, respectively, and the function Y is

$$Y = \frac{\alpha_H^2}{\alpha_P^2 + \tan^2 kL} . \tag{42}$$

We note that when $\alpha_H = 0$, Eq. (41) coincides with Eq. (36). The real and imaginary parts of x_0 for the fundamental mode are shown in Fig. 3 with the dashed lines (F mode) (cf. numerical calculations of Eq. (20) shown with solid lines for F mode). The small peaks in γ, seen in Figs. 3b and c, are due to the interference of the shear and compression modes. They disappear when $\alpha_H = 0$ and the modes are decoupled.

It should be noted that the shear Alfvén mode attenuation is much greater than that of the fast mode (Figs. 4 and 6). It means that the excitation of the fast mode in the IAR is quite possible and can play an important role in the formation of the IAR spectrum.

5 Excitation of resonance cavity by high-altitude wind

In order to obtain the spectrum of the EM perturbations, a specific form for the velocity distribution is required. There are a number of causes that affect the velocity spectrum at high altitudes, including the wind variations, internal gravity wave propagation, diurnal and seasonal variations, etc. For the sake of simplicity we assume that the neutral gas velocity has the form

$$\mathbf{v} = \mathbf{v}_0 + \delta\mathbf{v}, \quad \delta\mathbf{v} = \mathbf{v}_m \exp[i\mathbf{k}_0 \cdot (\mathbf{r} - \mathbf{U}t)] , \tag{43}$$

where $\mathbf{v}_0$ is the stationary neutral gas flow and $\delta\mathbf{v}$ is its variation, $v_m < v_0$. We consider that these variations propagate horizontally with constant speed $\mathbf{U}$ parallel to the wave vector $\mathbf{k}_0$. The value of $\mathbf{U}$ can be close to the velocity of internal gravity wave. In what follows we are interested solely in velocity variations $\delta\mathbf{v}$. The temporal Fourier transform of Eq. (43) is

$$\delta\mathbf{v}(\omega, \mathbf{r}) = \frac{\mathbf{v}_m \exp(i\mathbf{k}_0\mathbf{r})}{i(\omega - \mathbf{k}_0 \cdot \mathbf{U})} . \tag{44}$$

A spatial Fourier transform of Eq. (44) has the pole which corresponds to $\mathbf{k} = \mathbf{k}_0$. Substituting $\delta\mathbf{v}$ into Eqs. (14)–(15) and performing an integration over $\mathbf{k}$ one obtains the inverse Fourier transform of Eq. (14). As a result one can find $\delta\mathbf{B}$ as a function of ω, i.e. the spectrum of the geomagnetic variations. In order to find the contribution of the pole $\mathbf{k} = \mathbf{k}_0$ to the spectrum, one can formally replace $\mathbf{k}$ by $\mathbf{k}_0$ in Eqs. (14)–(19).

For a large-scale flow pattern the neutral gas should be considered practically incompressible, i.e. $\nabla \cdot \delta\mathbf{v} = 0$ (Kelley, 1989). Hence, $\mathbf{k}_0 \cdot \delta\mathbf{v} = 0$ so that $\mathbf{k}_0$ is orthogonal to $\delta\mathbf{v}$. Finally, we arrive at

$$Q = \frac{iL(\mathbf{k}_0 \times \mathbf{v}_m)_z \beta_1 \alpha_P}{v_{AI}(\omega - \mathbf{k}_0 \cdot \mathbf{U})} . \tag{45}$$

Substituting Eq. (45) into Eq. (14) one obtains the spectrum of geomagnetic variation caused by the wind motion Eq. (43) in the lower ionosphere at $90 - 120\,\mathrm{km}$. In order to illustrate the basic features of this spectrum, the numerical calculations have been carried out. We note that the power spectrum of the time-derivative of magnetic perturbations, i.e. $\omega|\delta\mathbf{B}|$, is usually recorded in the in-situ measurements. It is customary to normalize this spectrum by the value $\Delta t^{1/2}$, where Δt is the sample time (in s). The power spectrum of horizontal component, i.e. $\omega|\delta\mathbf{B}_\perp|/(\Delta t)^{1/2}$, in $\mathrm{T} \cdot \mathrm{Hz}^{1/2}$, as the function of frequency $f = \omega/2\pi$ is depicted in Fig. 4. Here ω stands for the real part of the wave frequency, the external magnetic field is $B = 5 \times 10^{-5}\,\mathrm{T}$, and other parameters are the same as in Fig. 3. Furthermore, $v_m = 50\,\mathrm{m/s}$, $U = 500\,\mathrm{m/s}$ and $\Delta t = 400\,\mathrm{s}$. For the daytime ionosphere (Fig. 4a) the height-integrated conductivities are $\Sigma_P = 5\,\mathrm{Ohm}^{-1}$ and $\Sigma_H = 7.5\,\mathrm{Ohm}^{-1}$, whereas for the nighttime conditions (Fig. 4b) these values are $\Sigma_P = 0.2\,\mathrm{Ohm}^{-1}$ and $\Sigma_H = 0.3\,\mathrm{Ohm}^{-1}$. In these figures the solid and dotted lines correspond to the wave numbers $k_0 = 0.01$ and $0.02\,\mathrm{km}^{-1}$, respectively.

According to Figs. 4a and b the decrease in k_0 results in the enhancement of the power spectra and the magnitude of the spikes. This follows from the fact that the denominator in Eq. (14) contains β_3 (19), which includes $\exp(k_0d)$, so that if $k_0d \gg 1$, the signals become practically undetectable owing to their smallness on the ground. For the daytime conditions and the wave numbers within 0.01–$0.02\,\mathrm{km}^{-1}$ the magnitude of the first spike is of the order of 60–180 pT/Hz$^{1/2}$. However, it is only a rough estimation of the magnitude because the latter strongly depends on k_0, the source spectrum and on other parameters. The spectrum oscillations seen in this figure are mainly due to oscillations in β_1 in the numerator of Eq. (45). The poles
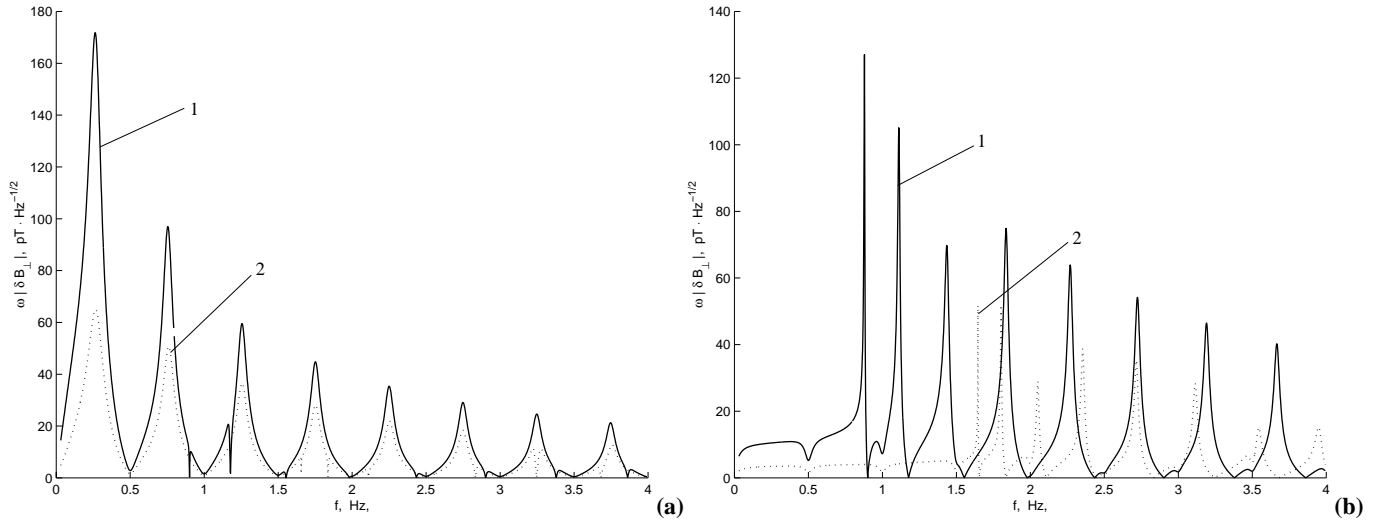
Fig. 4. A normalized power spectrum of the horizontal magnetic field at the ground level. **(a)** – daytime conditions, **(b)** – nighttime conditions. The solid line (1) and the dotted line (2) correspond to k_0=0.01 and 0.02 km^{-1}, respectively.

and zeros of this function are located close to the real axis of ω. If ω is purely real, the maxima in β_1 lie approximately at $x_0 \approx \pi \, (n-0.5)$, where n=1, 2..., or at the frequencies $f \approx 0.5 \, (v_{AI}/L) \, (n-0.5) = 0.5 \, (n-0.5)$ Hz. It should be noted that these values are very close to the IAR eigenfrequencies (shear mode) for the daytime conditions Eq. (37).

Such a coincidence of the characteristic frequencies is typical only for the daytime conditions. The nighttime IAR eigenfrequencies (shear mode) f=0.5n Hz (see Eq. (38)) correspond to the minima rather than to the maxima of the spectrum in Fig. 4b.

Comparison of the day- and nighttime power spectrums shows that, except for the first spike, the other spikes of the daytime spectrum are smaller than those of the nighttime spectrum. The nighttime conditions are thus more preferable for the IAR spectrum observation. This conclusion agrees with the results by Bösinger et al. (2002), who have recently reported the data of the first half year of operation of a sensitive search coil magnetometer at a remote site in the island of Crete, Greece (35.15° N, 25.20° E). It was shown that the spectral resonance structures (SRS) observed at these latitudes is a purely nighttime phenomenon.

In what follows we are mainly interested in the nighttime power spectrum. The nighttime spectrum shown in Fig. 5 was obtained with the use of the same parameters as before and L=10^3 km. Here the faster oscillations are seen in comparison with Fig. 4b, where the value L=500 km was used in a numerical simulation. The spikes in the nighttime spectrum are due to the fast mode. In order to estimate the frequencies of these spikes, we make use of an analytic approximation for the fast mode eigenfrequencies (see Eq. (41))

$$f_n \approx \frac{v_{AI} k_0}{2\pi} \left(1 + \frac{\pi^2 n^2}{2 k_0^2 L^2}\right),$$

where,

$$\frac{\pi^2 n^2}{2 k_0^2 L^2} \ll 1. \tag{46}$$

For L=10^3 km and k_0=0.01 km^{-1} we obtain $f_1 \approx 0.84$ Hz, $f_2 \approx 0.95$ Hz and $f_3 \approx 1.15$ Hz. This is close to the first three spikes in Fig. 5 (line 1). The appearance of the sharp spikes is due to the change in $\lambda_I = \left(k_0^2 L^2 - x_0^2\right)^{1/2}$. The first sharp spike arises as the frequency ω is greater than the threshold value $k_0 v_{AI}$, so that λ_I becomes purely imaginary. For example, when k_0=0.01 and 0.02 km^{-1}, the critical frequencies $f = k_0 v_{AI} / (2\pi) \approx 0.8$ and 1.6 Hz, respectively. This agrees with the numerical simulation given in Figs. 4b and 5 with lines 1 and 2.
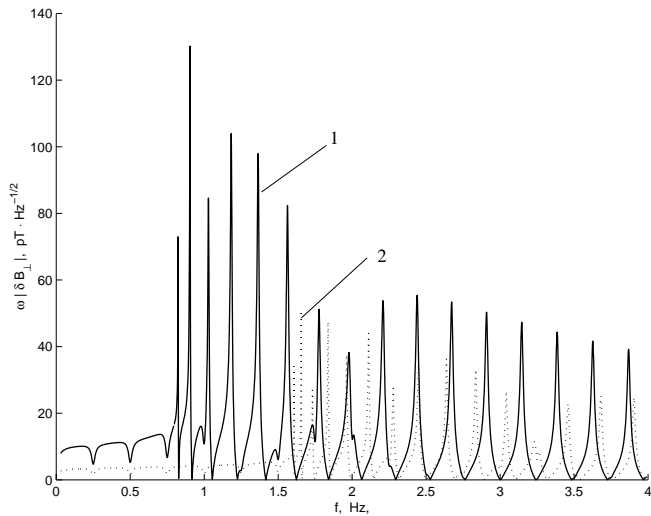
Bösinger et al. (2002) have found that the average frequency difference Δf between two adjacent quasi-harmonics in SRS is very small (0.2 Hz). Just the same average frequency difference can be seen in Fig. 5.

Interestingly enough the low frequency part of the nighttime spectrum does not contain the peaks, in spite of the fact that excitation of the shear mode at f=0.5 Hz (L=500 km, Fig. 4b) or f=0.25, 0.5 and 0.75 Hz (L=10^3 km, Fig. 5) may be expected. This peculiarity of the spectra is due to a specific form of Q (Eq. (45)). We recall that this form of Q results from the fact that the wave vector $\mathbf{k}_0$ is perpendicular to the wind velocity $\delta \mathbf{v}$. In order to illustrate this we consider the opposite case when $\mathbf{k}_0$ is parallel to $\delta \mathbf{v}$. Then Q is given by
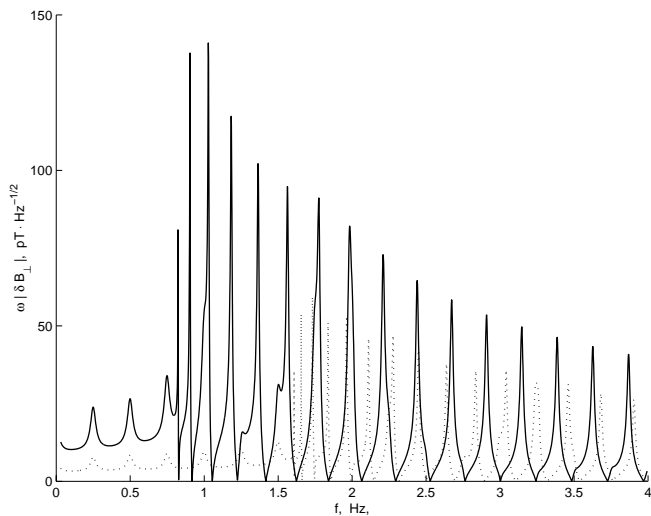
$$Q = -\frac{i L (\mathbf{k}_0 \cdot \mathbf{v}_m) \left(\alpha_H^2 + \alpha_P^2 + \beta_1 \alpha_P\right)}{v_{AI} (\omega - \mathbf{k}_0 \cdot \mathbf{U})}. \tag{47}$$

Figure 6 shows the nighttime spectrum obtained with the help of Eq. (47). For clarity the value L=10^3 km and the above parameters were used in a numerical simulation. The spikes

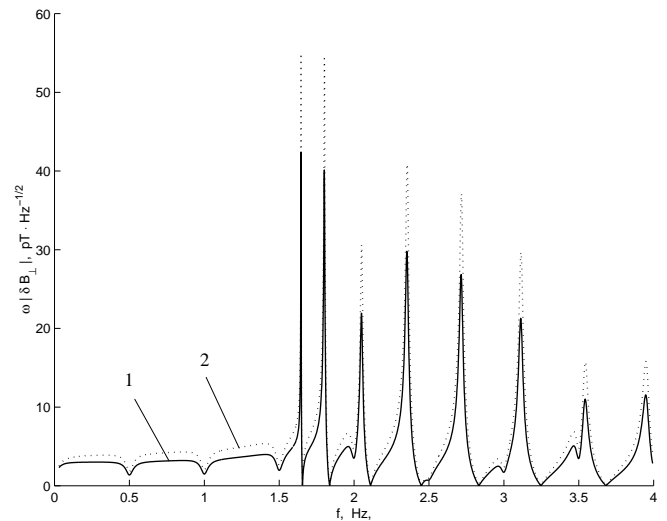**Fig. 5.** Same as in Fig. 4 but for $L=10^3$ km.

Fig. 6. The nighttime power spectrum at the ground level in the case when the wave vector $\mathbf{k}_0$ is parallel to the wind velocity $\delta\mathbf{v}$.

Fig. 7. Dependence of the nighttime power spectrum at the ground level on the ground conductivity. The solid line 1 corresponds to $\sigma_g=0$ and the dashed line 2 corresponds to $\sigma_g=10^{-2}$ S/m.

Polyakov and Rapoport, 1981; Lysak, 1991; Trakhtengertz and Feldstein, 1991; Pokhotelov et al., 2000, 2001).

Our numerical simulations show that the nighttime spectrum varies drastically due to the excitation of the fast mode when the frequency exceeds a value $f_0 \sim k_0 v_{AI}/(2\pi)$. The strong spikes whose frequencies depend on k arise in the frequency domain $f > f_0$. The attenuation of the fast mode is much smaller than that for the shear Alfvén wave. The horizontal propagation of the fast mode in the ionospheric waveguide in the F-layer has been studied by Greifinger and Greifinger (1968), who noted that the wave propagation in the ionospheric waveguide is more favorable during nighttime conditions. Our results agree with this conclusion in spite of the fact that we consider the vertical propagation of the two coupled modes across the waveguide rather than horizontal spreading of the fast mode. Thus, we conclude that excitation of the fast mode can play an important role in the formation of the nighttime IAR spectrum.

6 Discussion and conclusions

It is of common knowledge that traditional mechanisms of the IAR excitation, such as feedback instability, become less important in the mid- and low-latitudes. In these regions of the ionosphere the electric fields are basically generated by neutral winds (Kelley, 1989). As a result, we have restricted our consideration to high-altitude winds. In part, this mechanism is similar to acoustic autovibration in such a system as "a police whistle". Indeed, let us imagine a cylindrical case/shell bounded from one end and opened from another. It is known that an aerial flux externally tangent to the open end of the shell results in excitation of the aerial column eigenmodes. In such a case the energy flux coming from the external source is governed solely by the aerial column. The

at f =0.25, 0.5 and 0.75 Hz seen in the figure are due to the shear Alfvén mode, contrary to Fig. 5, where these spikes are absent. Comparison of Figs. 5 and 6 shows that the low frequency part of the spectrum substantially depends on the neutral wind properties.

Finally, Fig. 7 illustrates the dependence of the spectrum on the ground conductivity for the nighttime condition (here k_0=0.02 km^{-1}). The solid line corresponds to σ_g=0 and the dotted line corresponds to σ_g=10^{-2} S/m. As one sees from Fig. 7, the presence of the finite ground conductivity results in the enhancement of the several spectrum peaks.

Figures 4–7 show that the peaks of the shear Alfvén mode arising in the low frequency part of the nighttime power spectrum in the form of single or multiple spikes at the frequencies practically do not depend on the wave number. These spikes can be associated with the ordinary IAR spectrum (cf.

fluctuations of the tangent aerial flux whose frequencies are close to the aerial column eigenfrequencies in the shell can give rise to enhancement of the eigenmode magnitudes.

Our analysis shows that a similar scenario may operate in the ionospheric resonance cavity. In this case the neutral wind in the lower ionosphere can serve as an energy source for the cavity excitation. First, the part of the gas kinetic energy is transferred into the energy of the electric current in the conductive ionospheric slab, which is then converted into the energy of the shear and fast modes. Some of this energy is lost/dissipated due to the ionospheric Joule heating and wave energy leakage into the magnetosphere.

The fluctuations of the neutral wind can result in the enhancement of the energy flux flowing from the wind into the resonance cavity if the fluctuation frequency range is close to the IAR eigenfrequencies. Such fluctuations, which arise from the gas turbulence, are usually observed in the vicinity of the turbopause and they can occur in the E-layer. In order to find the frequency range that is typical for the turbulent pulsations, one needs a rough estimation of the neutral wind parameters. The gas flow pattern is characterized by the Reynolds number $Re = \Delta v \lambda \rho / \xi$, where ρ is the neutral gas mass density, Δv denotes the variation of the mean gas velocity and λ is the characteristic scale of the variations. The gas viscosity ξ due to molecular collisions can roughly be estimated as $\xi \sim (k_B T m)^{1/2} / \sigma_c$, where k_B is a Boltzmann constant, T is the gas temperature, m denotes the average ion mass and σ_c is the collisional cross section of the neutral particles. At the altitudes of the E-layer (100–130 km) the average ion mass is $m \approx 27$–28 units of proton mass that approximately corresponds to nitrogen molecular with $\sigma_c \sim 0.8 \times 10^{-18}$ m^2. Using these parameters one can find the rough estimation $\xi \sim 1.6 \times 10^{-5}$ Pa·s. We note that due to the interaction between eddies in the flow located below turbopause, the effective viscosity can be much larger than the molecular viscosity calculated above (Kelley, 1989). Our estimation is rather relevant to the E-layer where the turbulent mixing gradually decreases.

The neutral particle number density N decreases drastically with the altitude so that $N \sim (1 \times 10^{19} - 7 \times 10^{17})$ m^{-3} within the height interval under consideration. Choosing $N = 2 \times 10^{18}$ m^{-3} as an average value one obtains $\rho = Nm \approx 9 \times 10^{-8}$ kg/m^3. The wind speed is subject to diurnal and seasonal variations. For example, the diurnal wind variations increase with altitude from $10 - 30$ m/s at 95 km up to $100 - 150$ m/s at 200 km. So the value $\Delta v \sim (10 - 100)$ m/s seems to be a relevant estimation for the wind velocity fluctuations at the altitudes of $100 - 130$ km. Taking $\lambda \sim (1 - 10)$ km as a characteristic spatial scale of such fluctuations, one finally obtains $Re \sim 60 - 6 \times 10^3$.

With this estimation in mind, one can assume that such a great value of the Reynolds number exceeds the critical value that is necessary for transition from the laminar to a turbulent regime. The latter can give rise to the turbulence of the gas flow. The Kolmogorov theory (cf. Landau and Lifshits, 1986) assumes that if a neutral flow is stirred at some wavelength λ, certain structures will be formed in a so-called "in-

ertial subrange" in k space, where the energy will cascade to larger and larger values of k, i.e. from large to small scales. The cascade is bounded from below by the value λ^{-1} and from above by the so-called Kolmogorov dissipative scale $k_m = \lambda^{-1} Re^{3/4}$, where the influence of the molecular viscosity becomes significant and the energy dissipation occurs. So within the interval $\lambda^{-1} \ll k \ll \lambda^{-1} Re^{3/4}$ the energy is transferred from eddy to eddy with no net energy gain or loss. In an isotropic homogeneous medium the omnidirectional spectral density of the mechanical energy of the turbulent flow has a power law spectrum $\propto k^{-5/3}$. The typical frequencies of turbulent pulsations are evaluated as $\omega \sim kv$, where v is the smoothed mean velocity that slowly varies along the flow. Hence, we find that Kolmogorov spectrum is localized in the frequency range given by

$$\frac{v}{\lambda} \ll \omega \ll \frac{v}{\lambda} Re^{3/4},$$

where the lower margin corresponds to large-scale pulsations whereas the upper one stands for the dissipative turbulence scale, i.e. for the smallest pulsations in the turbulent flux. For instance, taking the parameters $v = 100$ m/s, $\Delta v = 50$ m/s and $\lambda = 10$ km one obtains $0.01 \ll \omega \ll 4$ Hz.

These estimations show that the typical frequency band of the gas flow turbulence can be close to the eigenfrequencies of the ionospheric resonance cavity that results in the most effective transition of the gas kinetic energy into the hydromagnetic wave energy. The numerical calculations show that the magnitude of the power spectrum can be detectable at ground level in spite of the energy dissipation due to Joule heating and wave leakage into the magnetosphere.

Our analysis shows that the IAR dispersion relation comprises of two modes. The first one corresponds to the ordinary shear Alfvén wave propagating along the geomagnetic field. Its spectrum practically does not depend on the perpendicular wave number k. However, the corresponding damping rate increases with the increase in k. The second mode corresponds to the fast mode and its eigenfrequency and damping rate strongly depend on k. The latter is one or two orders of magnitude smaller than that for the shear Alfvén wave. For the actual plasma conditions both modes are linearly coupled through the E-layer Hall conductivity. In particular, the periodic enhancement of the damping rate of the fast mode, seen in Figs. 3b and d when $k \approx \pi n / L$ (n is an integer), can be explained by this coupling. Except for the first spike, the magnitude of the daytime power spectrum is found to be lower than that of the nighttime spectrum. A few small spikes in the low-frequency part of the nighttime spectrum can be associated with the shear mode, whereas the series of strong spikes whose frequency exceeds a certain threshold value can be due to the fast mode. We can suppose that, namely, the fast mode can play an important role in the formation of the nighttime IAR spectrum.

Summarizing, we note that:

1. The IAR excitation at the mid-latitudes can be associated with the turbulent motions of the neutral winds. The

estimations show that this mechanism is capable of producing observable geomagnetic perturbations on the ground.

2. The IAR dispersion relation comprises of two coupled modes, the shear Alfvén wave and the fast mode. The eigenfrequencies of the first mode practically do not depend on the perpendicular wave number k, whereas for the fast mode they approximately follow the linear dependence on k. The fast mode damping rate decreases with the increase in k while the shear mode exhibits the opposite dependence.

3. The IAR power spectra contain the peaks both due to the shear and fast modes. The day- and nighttime power spectra have essentially different shapes and magnitudes and thus strongly depend on the wind parameters and ground/ionosphere conductivities. The nighttime IAR excitation should be expected to be more intensive because the peaks of the nighttime spectra are found to be greater than those for the daytime conditions.

Appendix A

Following Pokhotelov et al. (2000) we introduce a dimensionless frequency $x_0 = \omega L / v_{AI}$. When $z > h = l + L$ only outgoing wave solutions of the Eqs. (9) and (10) should be retained

$$\Phi = C_1 \exp\left(i x_0 z / L\right), \tag{A1}$$

$$\Psi = C_2 \exp\left(\lambda_M z / L\right), \qquad \lambda_M = \left(k^2 L^2 - x_0^2 \varepsilon^2\right)^{1/2}, \tag{A2}$$

where C_1 and C_2 are arbitrary constants.

The sign of λ_M in Eq. (A2) for the fast mode should be chosen in a way to satisfy the so-called radiation condition at the magnetospheric end. Hence, for $x_0 > kL$ the imaginary part of λ_M has to be positive. The bifurcation points of this function and the corresponding cut in the complex x_0 plane are shown in Fig. 2.

The next range of altitudes ($l < z < h$) is characterized by the Alfvén velocity $v_A = v_{AI}$, where $v_{AI} \ll v_{AM}$. In this case the solutions of the Eqs. (9) and (10) are given by

$$\Phi = C_3 \exp\left(i x_0 z / L\right) + C_4 \exp\left(-i x_0 z / L\right) \tag{A3}$$

$$\Psi = C_5 \exp\left(\lambda_I z / L\right) + C_6 \exp\left(-\lambda_I z / L\right), $$

$$\lambda_I = \left(k^2 L^2 - x_0^2\right)^{1/2}, \tag{A4}$$

where $C_3 - C_6$ are arbitrary constant quantities.

Faraday's law and the continuity of $\delta \mathbf{B}$ and $\mathbf{E}$ at the boundary $z = h$ require that the scalar potentials, Φ and Ψ, as well as their derivatives, $\partial_z \Phi$ and $\partial_z \Psi$, must be continuous at $z = h$. Using these conditions and Eqs. (A1)–(A4) one can express the constants $C_3 - C_6$ through $C_1 - C_2$. Then the solution of the Eqs. (A3) and (A4) can be rewritten in the form ($l < z < h$)

$$\Phi = \frac{C_1}{2} \exp\left(\frac{i x_0 h}{L}\right) \left\{ (1 + \varepsilon) \exp\left[-i x_0 \frac{(h - z)}{L}\right] \right.$$
$$\left. + (1 - \varepsilon) \exp\left[i x_0 \frac{h - z)}{L}\right] \right\} \tag{A5}$$

$$\Psi = \frac{C_2}{2} \exp\left(\frac{\lambda_M h}{L}\right) \left\{ \left(1 - \frac{\lambda_M}{\lambda_I}\right) \exp\left[\frac{\lambda_I (h - z)}{L}\right] \right.$$
$$\left. + \left(1 + \frac{\lambda_M}{\lambda_I}\right) \exp\left[-\frac{\lambda_I (h - z)}{L}\right] \right\}, \tag{A6}$$

where $\varepsilon = v_{AI} / v_{AM}$. Similar conditions should be applied at $z = l_{+0}$. Eliminating C_1 and C_2 from Eqs. (A5) and (A6), one obtains the boundary condition at $z = l_{+0}$

$$\partial_z \Phi (l) = \frac{i x_0 \beta_1}{L} \Phi (l), \tag{A7}$$

$$\partial_z \Psi (l) = \lambda_I \beta_2 \Psi (l) / L, \tag{A8}$$

where β_1 and β_2 are given by the Eqs. (17) and (18).

Appendix B

The solution of Eq. (11) decays at infinity ($z \to -\infty$) and is ($z < -d$)

$$\Psi = C_0 \exp\left(æz\right), \qquad (\text{Re}\,æ > 0). \tag{B1}$$

The solution of Eq. (12) can be written as ($-d < z < 0$)

$$\Psi = C_7 \exp\left(-kz\right) + C_8 \exp\left(kz\right). \tag{B2}$$

The constants C_7 and C_8 in Eq. (B2) can be expressed through C_0 making an allowance for the continuity of Ψ and $\partial_z \Psi$ at the boundary $z = -d$. This yields ($-d < z < 0$)

$$\Psi = \frac{C_0}{2} \exp\left(-æd\right) \left\{ \left(1 + \frac{æ}{k}\right) \exp\left[k (z + d)\right] \right.$$
$$\left. + \left(1 - \frac{æ}{k}\right) \exp\left[-k (z + d)\right] \right\}. \tag{B3}$$

At the interface $z = 0$ between the atmosphere and the ionosphere we have

$$\partial_z \Psi (0) = k \Psi (0) \frac{æ + k \tanh (kd)}{k + æ \tanh (kd)}. \tag{B4}$$

Since the atmosphere is an insulator the parallel electric current j_z flowing from the ionosphere to the atmosphere vanishes at $z = 0$. Then from Ampere's law we obtain

$$\partial_z \Phi (0) = 0. \tag{B5}$$

Similar to Lysak (1991) and Pokhotelov et al. (2000) we use a thin E-layer approximation, i.e. $kl \ll 1$. Integration of Eq. (6) over E-layer gives

$$\partial_z \Phi (l) + i \frac{x_0 \alpha_P}{L} \Phi (l) = -\frac{x_0^2 \alpha_H v_{AI}}{L^2} \Psi (l)$$
$$+ \frac{x_0 B}{L k^2} \left[\alpha_P (\mathbf{k} \times \mathbf{v})_z + \alpha_H (\mathbf{k} \cdot \mathbf{v})\right], \tag{B6}$$

where $\alpha_P = \Sigma_P / \Sigma_w$ and $\alpha_H = \Sigma_H / \Sigma_w$ are the ratios of the height-integrated Pedersen and Hall conductivities to the wave conductivity $\Sigma_w = 1/(\mu_0 v_{AI})$ and all the functions are taken at $z = l_{-0}$. In addition, we have taken into account Eq. (B5). For the sake of simplicity, the wind velocity $\mathbf{v}$ is assumed to be independent of the z-coordinate.

Then integration of Eq. (7) across the E-layer gives

$$\partial_z \Psi(l) - \partial_z \Psi(0) + i\frac{x_0}{L}\alpha_P \Psi(l) = -\frac{\alpha_H}{v_{AI}}\Phi(l)$$
$$-\frac{iB}{v_{AI}k^2}\left[\alpha_H(\mathbf{k}\times\mathbf{v})_z - \alpha_P(\mathbf{k}\cdot\mathbf{v})\right].\qquad\text{(B7)}$$

In the thin E-layer approximation we have $\Psi(l)=\Psi(0)$. Substituting Eqs. (A7), (A8) and (B4) into Eqs. (B6)–(B7) and rearranging, one obtains

$$\Phi(l)(\beta_1+\alpha_P) = i\alpha_H v_{AI}\frac{x_0}{L}\Psi(0)$$
$$-\frac{iB}{k^2}\left[\alpha_P(\mathbf{k}\times\mathbf{v})_z + \alpha_H(\mathbf{k}\cdot\mathbf{v})\right],\qquad\text{(B8)}$$

$$(ix_0\alpha_P - s)\Psi(0) = -\frac{\alpha_H L}{v_{AI}}\Phi(l)$$
$$-\frac{iBL}{v_{AI}k^2}\left[\alpha_H(\mathbf{k}\times\mathbf{v})_z - \alpha_P(\mathbf{k}\cdot\mathbf{v})\right],\qquad\text{(B9)}$$

where s is given by Eq. (16). Eliminating $\Phi(l)$ from Eqs. (B8) and (B9), one obtains

$$\Psi(0) =$$

$$\frac{BL\left[(\mathbf{k}\cdot\mathbf{v})\left(\alpha_H^2+\alpha_P^2+\beta_1\alpha_P\right) - (\mathbf{k}\times\mathbf{v})_z\beta_1\alpha_P\right]}{k^2 v_{AI}\left[(is+x_0\alpha_P)(\beta_1+\alpha_P)+x_0\alpha_H^2\right]}.\qquad\text{(B10)}$$

From Eq. (B3) we find that

$$\Psi(-d) = \frac{2k\Psi(0)}{\left[(k+\text{æ})\exp(kd)+(k-\text{æ})\exp(-kd)\right]}.\qquad\text{(B11)}$$

Appendix C

For the shear Alfvén wave Eq. (20) reduces to

$$\exp(2ix_0) = -\left(\frac{1+\varepsilon}{1-\varepsilon}\right)\left[1+\frac{2}{G(x_0)}\right],\qquad\text{(C1)}$$

where

$$G(x_0) = \alpha_P - 1 + \frac{\alpha_H^2}{is(x_0)/x_0 + \alpha_P}.\qquad\text{(C2)}$$

When $\alpha_H=0$ Eq. (C1) coincides with Eq. (22). For the daytime conditions α_P and α_H are usually of the order of several units. Then from Eq. (C2) it follows that $|G|\gg 1$. Since $\varepsilon\ll 1$ we conclude that the right-hand side of Eq. (C1) is close to -1. As before we seek the solution of Eq. (C1) in the form $x_0=\eta+i\gamma$. Equating the arguments of the complex values on both sides of Eq. (C1), in the first approximation we find that $\eta=\pi(n-1/2)$, where $n=1,2\ldots$

For the nighttime conditions α_P and α_H are small and thus $G\approx -1$. Equating, as before, the arguments of both sides of Eq. (C1), in the first approximation we obtain that $\eta=\pi n$. Equating the moduli of both sides of Eq. (C1) gives

$$\gamma = -\varepsilon - \frac{1}{2}\ln\left|1+\frac{2}{G(x_0)}\right|.\qquad\text{(C3)}$$

It follows from the analysis and numerical calculation shown in Fig. 4 that $\gamma\ll\eta$. So we can substitute η for x_0 in the function G in order to find γ in the next approximation.

Now let us study the fast mode. In this case Eq. (20) reduces to

$$\exp(2\lambda_I) =$$

$$\frac{(\lambda_M+\lambda_I)\left[\alpha_P+\alpha_H^2/(\beta_1+\alpha_P)+\alpha_g-i\lambda_I/x_0\right]}{(\lambda_M-\lambda_I)\left[\alpha_P+\alpha_H^2/(\beta_1+\alpha_P)+\alpha_g+i\lambda_I/x_0\right]},\qquad\text{(C4)}$$

where α_g is defined in Eq. (27).

When $\alpha_H=0$ Eq. (C4) coincides with Eq. (26) of Sect. 4.2. Again, when $kL\gg 1$ we apply the successive approximation method to find the solution of Eq. (C4). The function λ_I takes the form Eq. (29) and other functions including in Eq. (C4) should be taken in the first approximation at $x_0=kL$. Hence, $\lambda_M=kL$ and α_g is the same as that given by Eq. (32), i.e. $\alpha_g=\alpha_0$. Taking into account that x_0 is real, the function β_1 can be written as

$$\beta_1 = \frac{\varepsilon - i\tan kL}{1-i\varepsilon\tan kL} \approx -i\tan kL.\qquad\text{(C5)}$$

Substituting these functions and Eq. (C5) into Eq. (C4), one obtains that the right-hand side of Eq. (C4) can be expressed in terms of the power series of a small parameter $\lambda_I/(kL)$

$$\exp(2\lambda_I) =$$

$$1 + \frac{2\lambda_I}{kL}\left[1 - \frac{i}{\alpha_P+\alpha_0+\alpha_H^2/(\alpha_P-i\tan kL)}\right].\qquad\text{(C6)}$$

For $\alpha_H=0$ Eq. (C6) coincides with Eq. (31). Decomposing λ_I and α_0 into their real and imaginary parts, i.e. $\lambda_I=\lambda_1+i\lambda_2$ and $\alpha_0=\alpha_1+i\alpha_2$, equating the moduli and arguments of both sides of Eq. (C7), we arrive at the equations for λ_1 and λ_2

$$\lambda_1\left(1-\frac{p_1}{kL}\right) = \frac{\lambda_2 p_2}{kL},\qquad\text{(C7)}$$

and

$$\lambda_2\left(1-\frac{p_1}{kL}\right) = \pi n - \frac{\lambda_1 p_2}{kL},\qquad\text{(C8)}$$

where n is an integer and we made use of the following abbreviation

$$p_1 = 1 - (\alpha_2 + Y\tan kL)/p_3,\qquad\text{(C9)}$$

$$p_2 = [\alpha_P(1+Y)+\alpha_1]/p_3,\qquad\text{(C10)}$$

$$p_3 = [\alpha_P(1+Y)+\alpha_1]^2 + [\alpha_2+Y\tan kL]^2,\qquad\text{(C11)}$$

$$Y = \frac{\alpha_H^2}{\alpha_P^2 + \tan^2 kL}.\qquad\text{(C12)}$$

Substituting solution of Eqs. (C7) and (C8) into Eq. (30), one obtains the equations for δ_1 and γ_1. Finally, one finds

$$x_0^n = kL + \frac{\pi^2 n^2}{2kL[1-p_1/(kL)]^2}\left\{1-\frac{2ip_2}{kL[1-p_1/(kL)]}\right\},\qquad\text{(C13)}$$

where p_1 and p_2 are given by Eqs. (C9)–(C12). When $\Sigma_H=0$ this solution coincides with that given by Eq. (36).

References

Andronov, A. A. and Trakhtengerts, V. Y.: Kinetic instability of outer Earth's radiation belts, Geom. Aeron., 4, 233–242, 1964.

Belyaev, P. P., Polyakov, S. V., Rapoport, V. O., and Trakhtengertz, V. Y.: Discovery of the resonance spectrum structure of atmospheric EM noise background in the range of short-period geomagnetic pulsations, Dokl. Akad. Nauk SSSR, 297, 840–843, 1987.

Belyaev, P. P., Polyakov, S. V., Rapoport, V. O., and Trakhtengertz, V. Y.: The ionospheric Alfvén resonator, J. Atmos. Terr. Phys., 52, 781–787, 1990.

Belyaev, P. P., Bösinger, T., Isaev, S. V., and Kangas, J.: First evidence at high latitudes for the ionospheric Alfvén resonator, J. Geophys. Res., 104, 4305–4317, 1999.

Bespalov, P. A. and Trakhtengerts, V. Y.: The cyclotron instability in the Earth radiation belts, Pub. Plenum, edited by Leontovich, M. A., New York, Vol. 10, 155–192, 1986.

Bösinger, T., Haldoupis, C., Belyaev, P. P., Yakunin, M. N., Semenova, N. V., Demekhov, A. G., and Angelopoulos, V.: Spectral properties of the ionospheric Alfven resonator observed at a low-latitude station (*L*=1.3), J. Geophys. Res., 107, 1281, doi:10.1029/2001JA005076, 2002.

Chaston, C. C., Carlson, C. W., Peria, W. J., Ergun, R. E., and McFadden, J. P.: Fast observations of the inertial Alfvén waves in the dayside aurora, Geophys. Res. Lett., 26, **,** 647–650, 1999.

Chaston, C. C., Bonnell, J. W., Carlson, C. W., Berthomier, M., Peticolas, L. M., Roth, I., McFadden, J. P., Ergun, R. E., and Strangeway, R. J.: Electron acceleration in the ionospheric Alfvén resonator, J. Geophys. Res., 107, 1413, doi:10.1029/2002JA009272, 2002.

Chaston, C. C., Bonnell, J. W., Carlson, C. W., McFadden, J. P., Ergun, R. E., and Strangeway, R. J.: Properties of small-scale Alfvén waves and accelerated electrons from FAST, J. Geophys. Res., *108*, 8003, doi:10.1029/2002JA009420, 2003.

Demekhov, A. G., Trakhtengertz, V. Y., and Bösinger, T.: Pc 1 waves and ionospheric Alfvén resonator: generation or filtration?, Geophys. Res. Lett., 27, 3805-3808, 2000.

Fraser-Smith, A. C.: ULF magnetic fields generated by electrical storms and their significance to geomagnetic pulsation generation, Geophys. Res. Lett., 20, 467–470, 1993.

Greifinger, C. and Greifinger, S.: Theory of hydromagnetic propagation in the ionospheric waveguide, J. Geophys. Res., 76, 7473, 1968.

Grzesiak, M.: Ionospheric Alfvén resonator as seen by Freja satellite, Geophys. Res. Lett., 27, 923–926, 2000.

Hickey, K., Sentman, D. D., and Heavner, M. J.: Ground-based observations of ionospheric Alfvén resonator bands, EOS Trans, AGU, 77(46), Fall Meeting Suppl., F92, 1996.

Kangas, J., Guglielmi, A. V., and Pokhotelov, O. A.: Morphology and physics of short-period magnetic pulsations (A Review), Space Science Review, 83, 435-512, 1998.

Kelley, M. C.: The Earth's Ionosphere, Academic Press, INC, 487, 1989.

Kennel, C. F. and Petschek, H. E.: Limit on stability of trapped particle fluxes, J. Geophys. Res., 71, 1, 1966.

Landau, L. D. and Lifshits, E. M.: Hydrodynamics, Nauka, Moscow, 1986.

Lysak, R. L.: Feedback instability of the ionospheric resonator cavity, J. Geophys. Res., 96, 1553–1568, 1991.

Lysak, R. L. and Song, Y.: Energetics of the ionospheric feedback interaction, J. Geophys. Res., 107, 1160, doi:10.1029/2001JA00308, 2002.

Mishin, E. V., Burke, W. J., Huang, C. Y., and Rich, F. J.: Electromagnetic structures within subauroral polarization streams, J. Geophys. Res., 108, 1309, doi:10.1029/2002JA009793, 2003.

Onishchenko, O. G., Pokhotelov, O. A., Sagdeev, R. Z., Stenflo, L., Treumann, R. A., and Balikhin, M. A.: Generation of convective cells by kinetic Alfén waves in the upper ionosphere, J. Geophys. Res., 109, A03306, doi:10.1029/2003JA010248, 2004.

Pokhotelov, O. A., Pokhotelov, D., Streltsov, A., Khruschev, V., and Parrot, M.: Dispersive ionospheric Alfvén resonator, J. Geophys. Res.,105, 7737–7746, 2000.

Pokhotelov, O. A., Khruschev, V., Parrot, M., Senchenkov, S., and Pavlenko, V. P.: Ionospheric Alfvén resonator revisited: Feedback instability, J. Geophys. Res., 106, 25 813–25 824, 2001.

Pokhotelov, O. A., Onishchenko, O. G., Sagdeev, R. Z., and Treumann, R. A.: Nonlinear dynamics of the inertial Alfvén waves in the upper ionosphere: Parametric generation of electrostatic convective cells, J. Geophys. Res., 108, 1291, doi:10.1029/2003JA009888, 2003.

Pokhotelov, O. A., Onishchenko, O. G., Sagdeev, R. Z., Balikhin, M. A., and Stenflo, L.: Parametric interaction of kinetic Alfvén waves with convective cells, J. Geophys. Res., 109, A03305, doi:10.1029/2003JA010185, 2004.

Polyakov, S. V.: On the properties of the ionospheric Alfvén resonator, in: KAPG Symposium on Solar-Terrestrial Physics, Vol. 3, Nauka, Moscow, 72–73, 1976.

Polyakov, S. V., and Rapoport, V. O.: The ionospheric Alfvén resonator, Geomagn. Aeron., 21, 610–614, 1981.

Sukhorukov, A. I. and Stubbe, P.: Excitation of the ionospheric resonator by strong lightning discharges, Geophys. Res. Lett., 24, 829–832, 1997.

Streltsov, A. V. and Mishin, E. V.: Numerical modeling of localized electromagnetic waves in the nightside subauroral zone, J. Geophys. Res., 108, 1332, doi:1029/2003JA009858, 2003.

Trakhtengertz, V. Y., and Feldstein, A. Y.: Turbulent Alfvén boundary layer in the polar ionosphere, 1, Excitation conditions and energetics, J. Geophys. Res., 96 , 19 363–19 374, 1991.